Experimental investigation of shear-driven water film flows on horizontal metal plate

M. Leng[a], S. Chang[a,*], H. Wu[b, **]

[a] School of Aeronautic Science and Engineering, Beihang University, Beijing 100191, China

[b] School of Engineering and Technology, University of Hertfordshire, Hatfield, AL10 9AB, United Kingdom

* Corresponding author. Email: sn_chang@buaa.edu.cn; Tel. +86(10) 8233 8008; Fax. +86(10) 8233 8008

** Corresponding author. Email: h.wu6@herts.ac.uk Tel. +44(0) 1707 284265; Fax. +44(0) 1707 285086

Abstract: In this article, an experimental investigation has been conducted to characterize the instantaneous thickness of the surface water film driven by high-speed airflow pertinent to aerodynamic icing and anti-icing modeling. Non-intrusive results of the film flowing on a metal plate were obtained using the high-speed camera and confocal chromatic technique. The wind speed (U_a) ranges from 17.8 m/s to 52.2 m/s, and the film Reynolds number (Re_f) ranges from 26 to 128. The effect of the high-speed airflow on the structure of the wave film was observed and analyzed qualitatively. A new correlation of the interfacial shear factor was

proposed for the prediction of the average film thickness. The predictions were compared with the previous annular flow models by applying the dimensionless analysis method and a good agreement is achieved. The superficial roughness, characterized by root-mean-square of the thickness, was well-correlated using a piecewise linear function of the average film thickness. Furthermore, a comprehensive description of the superficial waves including spectrum analysis and division of film thickness data between underlying film and large waves was presented. Transformations of the wave frequency and amplitude with the wind speed and the film Reynolds number were also addressed.

Keywords: Aerodynamics; shear-driven flow; interfacial shear factor; film thickness; wave statistics.

1. Introduction

Structural and aircraft icing usually occurs when supercooled droplets from clouds impact on the cold surface, causing performance degradation and even serious threat to safety [1, 2]. Droplets may freeze directly after impingement at lower temperature, building up fluffy rime ice. However, droplets may not completely freeze when the latent heat cannot be rapidly released into the ambient under glaze icing condition, or when the anti-icing system is working. The unfrozen part will redistribute the surface water, resulting in the accumulation of the ice outside the impingement area or protection area, severely changing the aerodynamic shape [3, 4]. At the same time, the disturbance on the interface between the air and water would introduce additional surface roughness [5], resulting in disturbed boundary layer flow and instability factor during ice accretion process. For the above reasons, the presence of the liquid water on the aerodynamic surface does not only raise the danger caused by the ice accretion, but also make the icing/anti-icing modeling more complex.

Messinger [6] model was the first successful trial to consider the flow of the

liquid water in predicting the ice accretion, and it was widely applied in numerical simulations. The developed model assumed that the unfrozen part completely went downstream due to the mass conservation, regardless of the shape state of the surface water. Through high speed videos taken in wind tunnel experiments [7, 8], it was observed that the water mass could be in a bead, film or rivulet state as a consequence of the presence of the water remaining stationary on the surface. The impinging droplets form beads on the surface, and then their water content is removed by wind or gravity. If much more water is present on the surface, the beads would coalesce into water film. The rivulets appear by the runback of the deformed beads, or the breakoff of the film beyond the collection area of the impinging droplets. Based on the experimental observations, several improvements have been proposed and examined from both a computational and analytical viewpoint [9, 10, 11]. But still some assumptions and approximations such as undisturbed boundary layer and uniform shear stress were made in their models, which introduced various limitations on the applicability of the predictions. To reveal the micro-physical mechanism and inherent laws behind the water transport behavior, some experimental investigations were carried out aiming at different water states respectively. For the bead, force analysis, shedding correlation and coalescence were obtained corresponding to the surface wettability, wind speed and bead volume [12, 13]. For the rivulet, the formation and breakoff criteria were studied, as well as the thickness, width and interval under different flow rate and wind speed were investigated [14, 15]. With respect to the film, which is frequently accounted for the main part on the airfoil surface, Feo and Tsao [16] obtained the film thickness at stagnation point using conductance sensor for the sake of scaling calculation. Muzik et al. [17] and Alzaili and Hammond [18] recorded the superficial images of the continuous film. Zhang et al. [19, 20] developed a technique based on the digital image projection (DIP) to observe the film thickness on an airfoil. It was concluded from their experimental results that the thickness of the film was at micro scale and accompanied with

high-frequency fluctuations, but the correlation between the film flowing and effect factors was still absent.

There are several characteristics of the water film, such as micro-scale thickness, complex interfacial waves, high-reflective surface, fast variation in time and space and easiness to be disturbed, which make the measurement of the thickness complicated. Although it was full of challenges, extensive investigations have been done regarding the liquid film issues using various techniques. Examples include the capacitance probe [21], laser focus displacement meter [22, 23], planar laser-induced fluorescence imaging [24, 25], conductance method [26], and optical measurement method [27, 28]. Majority of the previous experiments considered the gravity driven films or the two-phase flow in a vertical or horizontal tube, while few attentions were paid on the shear-driven film on the outer surface of the components. For shear-driven film flow in a large-scale space, which means the influence of the side and top walls could be neglected, there are few experimental results reported in the open literatures [25, 29]. Besides, a low dependency on the geometry of the flow duct is ideal for the validation of a computational fluid dynamic (CFD) code.

A flow model of the water film under aircraft icing condition has been derived by Myers [30, 31], in which multiple effect factors are obtained, including ambient pressure, surface tension, gravity and shear stress. Myers' model was then applied in glaze icing, runback ice ridge and anti-icing simulations [32, 33, 34, 35]. Among the several effect factors, interfacial shear stress was found to be a key factor to calculate the local film thickness, but it is difficult to be evaluated due to lack of the measured data. The most common substitute in CFD computations was the wall friction stress in boundary layer of the airflow, which was evaluated from the control volumes of the first layer near the body. Considering that the superficial fluctuations between the gas and liquid phases would strengthen the interfacial shear. Karev et al. [36] and Du et al. [33] applied the correlations from experiments of the stratified flow. In regarding to the surface roughness, the interval and height of the interfacial waves were usually

used as the characterization. Ueno and Farzaneh [37] separated the interfacial fluctuations from mean film thickness, and solved out the wavelength and amplification factor on the basis of the stability analysis theory. The recent study implemented by Rothmyers [38, 39] was to perform a simulation on the fully interaction of the air-water-ice field with surface waves and ice roughness presented. However, rather than these iteration modeling, an explicit empirical correlation for the superficial roughness was preferred in practical application [11].

It appears from the previous investigations that the water film flow plays an important role in aerodynamic icing and anti-icing problems, and the effect of the water film has been taken into account in recent prediction models. From an engineering perspective, however, there are still several hypotheses and speculations behind these models, especially the magnitude of the interfacial shear stress and the structure of the superficial fluctuations. More efforts need to be made for the experiments on the wind-driven film flows and on the outer surface of the structure. As such, the present research work aims to investigate the local instantaneous thickness of the film sheared by a high-speed airflow on a horizontal substrate. The motivation behind this work is to quantitatively understand the microphysical phenomenon behind the surface water transport behavior. The experimental apparatus and measurement method are described in Section 2, and the results are presented and analyzed in Section 3 ordered by time-dependent traces, mean film thickness and wave characteristics. Conclusions are summarized in Section 4.

2. Experimental apparatus and methods

Experiments were conducted in the open-loop ‘liquid film’ wind tunnel of Anti-icing/de-icing research laboratory in Beihang University, China, as shown in Fig. 1. The duct body of the wind tunnel, composed of the station section, contraction section, test section and diffuser section, is mounted on the support structure made by stainless steel and aluminum profile. The bottom of the test section is made of a steel

frame inlaid by aluminum sheet measuring 200 mm wide and 500 mm long, while the remaining three sides are made by acrylic glass, providing a full view of observation. The top wall is 50 mm apart away from the bottom. Airflow through the bottom and top walls is generated by a centrifugal blower an inverter motor. A honeycomb and two layers of gauzes are placed in the upstream duct of the contraction and test sections to make the exit flow uniform. The maximum velocity that can be produced by the blower in test section is 55 m/s. Wind speed was measured over the cross-area at measurement location using a Pitot tube anemometer with an accuracy of 0.1 m/s. The variation in wind speed over the middle 85% of the test section width measured about 2% of the mainstream speed.

The working fluid, distilled water, is driven by a submersible pump and passes through a supplement vessel before entering the test section at a distance of 55 mm from the inlet of test section. The water flow-rate was measured by pre-calibrated rotameter with an accuracy of 5%. The supplement vessel is made of Plexiglas which is ideal for sealing due to its unwettability. The distilled water slowly rises into the test section through a 100 mm length groove with a rounded edge at downstream side, and then flows forward along the aluminum surface driven by the airflow. At the end of the test plane, liquid is collected in a trap through a slot at the bottom of the substrate, which is filled with an absorbent sponge material to capture the water and prevent suction of the air. As an addition, an interception net is mounted at the end of the diffuser section to reduce the trouble caused by entrained droplets, but this part of water is not recycled.

The film thickness was measured using a laser focus displacement meter (ACR-HNDS100 produced by Schmitt Industries, Inc.) based on the chromatic aberrations technique. The sensor consists of a control unit and a measure head (optical pen), with a laser spot diameter of 34 μm, and focal point distance of 37.2 - 45.2 mm. The measurement point was located at the longitudinal centerline of the test plane and 245 mm downstream from the outlet of the water feeding reservoir, as

shown in Fig. 1(b). In all test conditions, the width of the film should not change before it reached the measurement location. In the film thickness measurement, a time record of 20,000 data points was collected for each run and then directly stored in the computer. The time interval between the data points was 0.0005 s. The linearity of the sensor output was calibrated as below 0.27%.

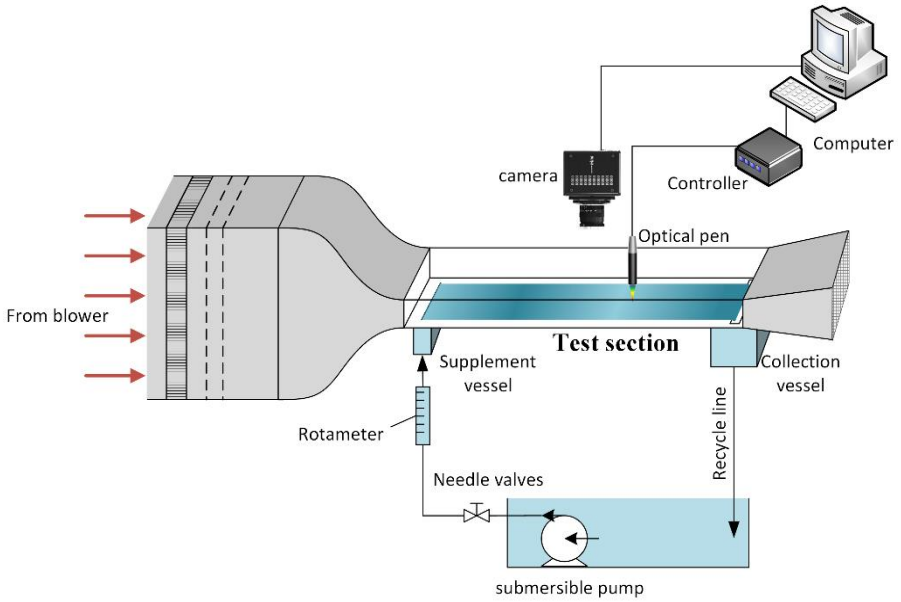

(a)

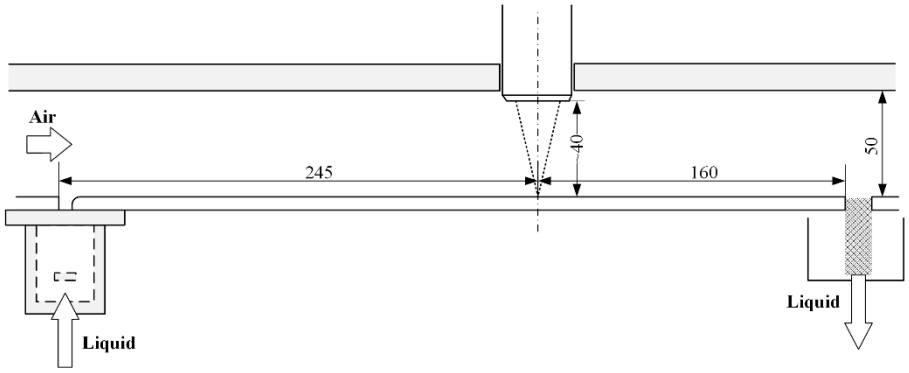

(b)

Fig. 1. Schematic diagram of experimental setup. (a) Flow loop; (b) Test section.

All the tests were carried out at room temperature and under stationary conditions. The wind speed varied between 17.8 m/s and 52.2 m/s, and the film Reynolds number, Re_f varied within the range of 26 -138. Re_f is defined as $Q/w\nu_l$.

Here Q is the volumetric liquid flow rate per width, ν_l is the kinematic viscosity of the liquid, and the width of the film, w, was measured from the photos that taken by camera and generally equal to the width of the aluminum sheet. The uncertainty in the film Reynolds number Re_f, which is affected by the measurement of the flow rate and the width of the test section surface, does not exceed ±5%. For wind speed and Reynolds number in the current range, a continuous film would be expected on the aluminum substrate. The surface of the aluminum was polished and cleaned with 95% alcohol before each group of tests. Initially, the distilled water was pumped into the supplied vessel. As soon as the wind speed reached a steady state, the water in the vessel was pumped into the test section through the groove. As a stable shear-driven liquid film was formed on the test surface, the sensor started to measure the film thickness. Each group of the experiments was repeated three times, and the results were averaged over the three repeats.

3. Results and discussion

3.1. Instantaneous film thickness

In this section, the local instantaneous film thickness recorded by the sensor will be used to provide an insight of the interfacial structure and its variation under different wind speed U_a and film Reynolds number Re_f. The experimental conditions are drawn in terms of U_a and Re_f shown in Fig. 2, as well as two close pictures of the water film, respectively representing two different flow regimes. The corresponding dynamic processes can be seen in Movie 1 and Movie 2. Two arrays of typical time-dependent traces of film thickness under different U_a and Re_f are respectively given in Figs. 3 and 4. Results show that the film consisted of underlying thin layer, small amplitude waves (ripples), and large-amplitude waves, also called roll waves. By taking into account the qualitative observation of the interfacial structure and quantitative analysis of the large waves, two types of flow regime are identified within current conditions, which are represented by different symbols as shown in Fig.

2:

(i) ‘3D wave’ regime, occurring at lower film Reynolds number, where the interface is covered by regular ripples, moving together with the underlying water film. Examples can be seen at the top three traces of Figs. 3 and 4. In the present study, the flow is identified as ‘3D wave’ regime when the frequency of the large amplitude waves is all less than 5 for all three repeats (details are given in sections 3.3.3).

(ii) ‘roll wave’ regime, also known as Kelvin-Helmholtz (K-H) wave, in which large amplitude waves irregularly appear above the ripples and underlying film. This regime can be seen in the cases of $Re_f > 64$ in Fig. 3 or $U_a < 42.2$ m/s in Fig. 4. The large waves advance faster than the ripples and base film, thus can travel across them and cause a certain impact.

Actually, a gradual variation is observed in the traces of the instantaneous film thickness with varying Re_f or U_a, rather than an instant transition. For example, the frequency of the large wave might be less than 5 or more than 5 in different experimental tests (but never more than 9), so there are two symbols mark at the same condition point in Fig. 2.

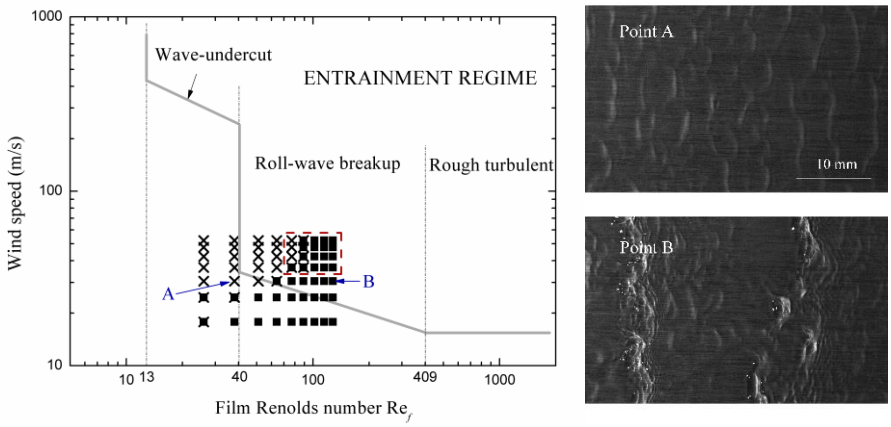

Fig. 2. Comparison of experimental points with the entrainment correlation for air-water flow at 20℃ (× represents ’3D wave’ regime; ■ represents ‘roll wave’ regime; Inner red dash line represents entrainment regime. Point A represents the experiment condition of U_a = 30.5m/s and Re_f = 38; Point B represents U_a = 30.5m/s and Re_f = 128).

For some cases of high U_a and Re_f, the entrained droplets were observed at the exit of the wind-tunnel. In order to evaluate the effect of the entrainment, the obtained experimental data were compared to the drop entrainment criteria from the work of Ishii and Grolmes [40], which was derived based on the force balance and stability theory, thus independent with the shape and size of the substrate. Comparison shows that the entrainment mainly occurs as the type of the roll-wave breakup, which means the tops of the large amplitude roll waves are sheared off from the crests by the high-speed gas stream. It was observed that the entrainment phenomenon was only dominative at the conditions when U_a was larger than 36.5 m/s and Re_f was larger than 77, which is consistent with Ishii's correlation. Besides, the entrained droplets were generally carried out by the high-speed airflow in horizontal plate experiment. Therefore, the following analysis will be concentrated on the residual surface water films, which is also the concern in structure and aircraft icing study.

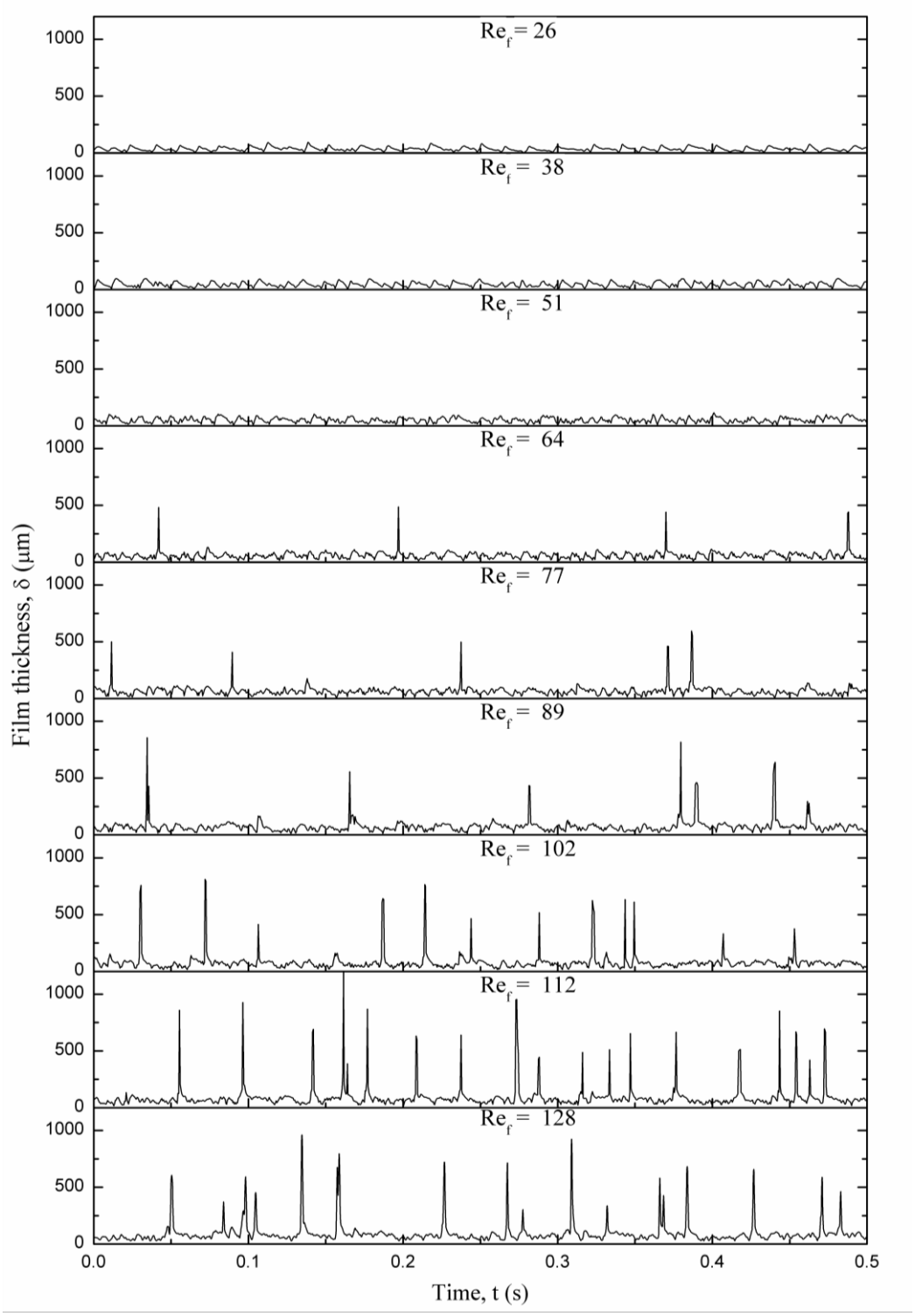

Fig. 3. Time traces of the local film thickness at measurement station for the air speed of 30.5 m/s.

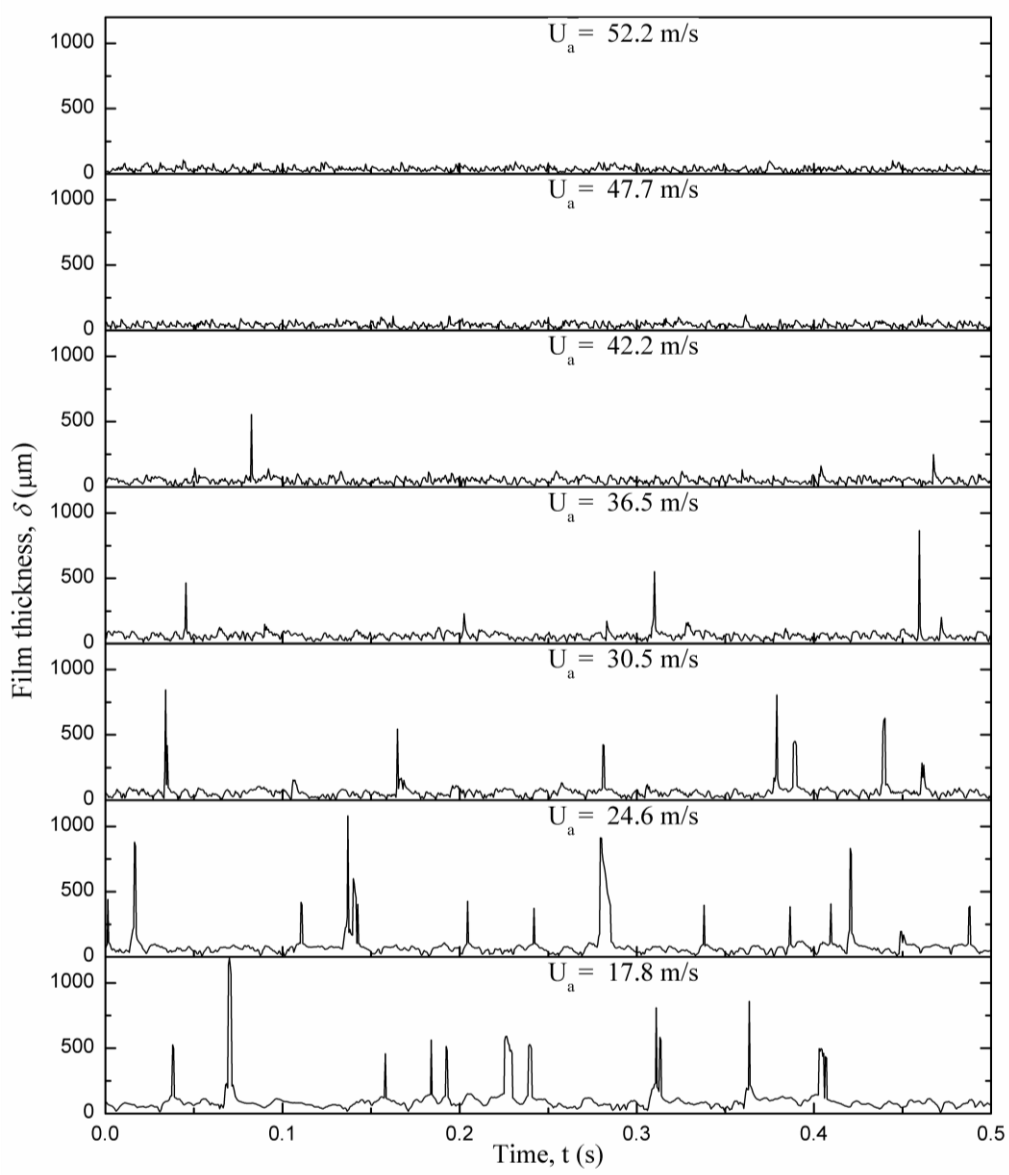

Fig. 4. Time traces of the local film thickness at measurement station for the film Reynolds number of 89.

Fig. 3 indicates how the large waves are generated as a function of the film Reynolds number Re_f when the wind speed is fixed at 30.5 m/s. Initially, the film is covered with ripples of the similar frequency for the smaller Reynolds number cases (Re_f = 26~51); then the wave length of the ripples slightly decreased with increasing flow rate, and quickly evolve into the larger waves at higher Reynolds numbers ($Re_f \geq$ 64). It is found that the thickness of the underlying layer and the superficial shapes are similar at different flow rates, and only the frequency of the large wave obviously

increases with increasing Re_f.

On the other hand, when the wind speed U_a varies, as shown in Fig. 4, both ripples and large waves show an obvious variation. The underlying water layer seems much thicker and has smooth surface for the smaller wind speed cases, such as U_a = 17.8 m/s, while the frequency of the superficial ripples on the underlying reaches the peak at maximum wind speed U_a = 52.2 m/s. The variations of the large waves with decreasing U_a are reflected not only in frequency but also in shape, the wider shape at smaller U_a indicates slower speed of the large wave.

3.2. Mean film thickness and superficial roughness

Fig. 5 shows the variations of the mean film thicknesses ($\overline{\delta} = \frac{1}{n}\sum_{i=1}^{n}\delta_i$) with (a) wind speed U_a and (b) film Reynolds number Re_f. From Fig. 5, gradual and consecutive trends are observed. In general, the mean film thickness $\overline{\delta}$ increases with decreasing wind speed or increasing film Reynolds number, but these dependences will have cross-impact. For the case of high wind speed, the dependence of the mean film thickness on Re_f declines. For instance, the mean film thickness for U_a = 17.8 m/s increases from 63 μm to 167 μm as the film Reynolds number varies from 26 to 128, while for the cases of maximum U_a, the thickness increases by 25 μm in the same range of Re_f. Similarly, for lower Re_f, the mean film thickness varies more slightly with wind speed.

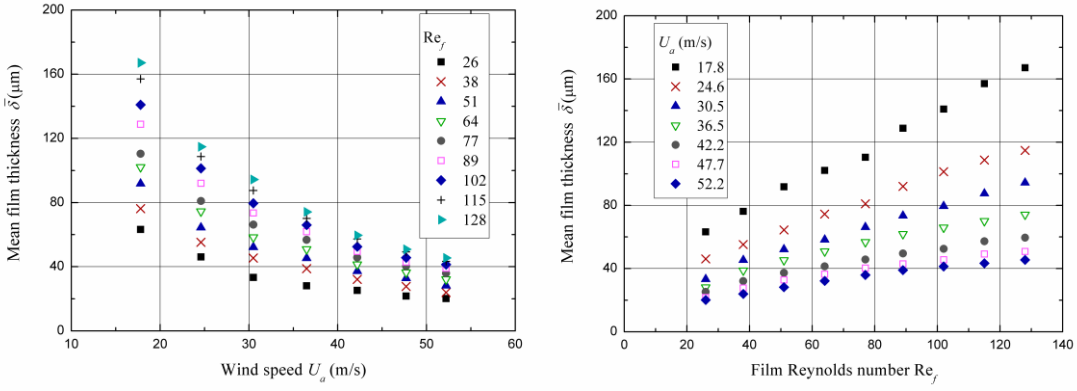

(a) (b)

Fig. 5. Mean film thickness under different (a) wind speed U_a and (b) film

Reynolds number Re_f.

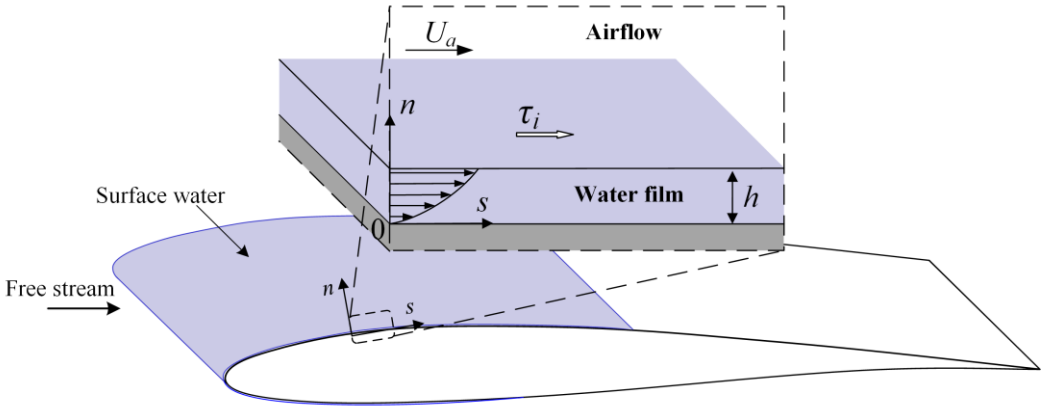

Fig. 6. Schematic diagram of water film flow model

A formula for predicting the thickness of a continuous water film on aircraft in icing conditions was first derived theoretically by Myers [30, 31], assuming that the film flow was stable. The model clarified the relationship between the interfacial shear stress and the equilibrium film thickness. As shown in Fig. 6, the equilibrium thickness of the water film flow is the real root of

$$2\rho_l g \sin\alpha \bar{\delta}^3 + 3\tau_i \bar{\delta}^2 = 6\mu_l Q \tag{1}$$

where g is the magnitude of the gravity acceleration, τ_i is the interfacial shear stress, ρ_l and μ_l are the density and dynamic viscosity, respectively, and Q is the liquid fluid flux per unit width. α is the inclined angle of the substrate. For horizontal cases, $\alpha = 0$, the film thickness is given as:

$$\bar{\delta} = \sqrt{\frac{2\mu_l Q}{\tau_i}} \tag{2}$$

It can be seen that the dynamic viscosity of liquid (μ_l) and the flow rate (Q) are both accessible parameters, as μ_l can be obtained from temperature, and Q equals flow-in water. Therefore, τ_i becomes the key factor to determine the film thickness. Based on the aerodynamic force formula, the shear force at the interface can be expressed by an interfacial friction factor:

$$\tau_i = f_i \frac{1}{2} \rho_a \left(U_a - C\right)^2 \tag{3}$$

where f_i is the interfacial shear factor, U_a is the wind speed, and C is the phase velocity of the superficial waves. It was reasonably assumed here that $U_a >> C$ for the interval cover by the wind speed and flow rate in this study [41, 42, 43]. Then the calculation of the interfacial shear stress will be

$$\tau_i = f_i \frac{1}{2} \rho_a U_a^2 \tag{4}$$

It can be seen that the interfacial shear factor on the water film surface, f_i, now becomes the only unknown factor for the prediction of film thickness. There have been several models to calculate the interfacial stress in previous studies of the aircraft icing prediction. Two mainstream calculations were Wall friction model and Stratified flow model [18, 33, 34, 36], which have been transferred into the expressions containing f_i here:

(i) Wall friction model

For numerical simulation of icing prediction, the computational process was generally developed by dividing the problem into three sub-processes, each representing a fictitious quasi-steady process. They were air flow field calculation, water droplet trajectory calculation, mass and energy balance calculation on the surface, respectively. With this premise, the air shear stress, as the main driving force acted on the water film flow, was obtained from an assumed undisturbed boundary layer. Therefore, the interfacial shear factor f_i, was considered equal to the wall friction factor c_f. A correlation for the local skin friction coefficient in turbulent boundary layer is used for representation here [44]:

$$f_i = c_f = 0.0578\left(\mathrm{Re}_a\right)^{-0.2} \tag{5}$$

where $\mathrm{Re}_a = U_a \cdot L / v_a$, and v_a is viscosity of air, L is the characteristic length and equals to the downstream distance here.

(ii) Stratified flow model

To take account the effect of the superficial fluctuations on the air shear,

improvements were made through introducing the correlations in existed stratified flow experiments [33, 36]. A typical correlation applied was Miya's model [45], which was summarized based on Cohen and Hanratty's experiment:

$$f_i = 0.0142 \qquad \mathrm{Re}_f < 100 \tag{6a}$$

$$f_i = 0.008 + 2\times10^{-5}\,\mathrm{Re}_f \quad 100 \le \mathrm{Re}_f \le 1700 \tag{6b}$$

These substitute models were validated through the macroscopic results, thus the error introduced by the interfacial shear factor could not be easily evaluated. Since even minor surface perturbations will lead to a considerable influence on the air boundary flow and would increase the interfacial shear stress, the best way to access the interfacial shear stress is by experiment.

Interfacial shear factor f_i was evaluated by substituting the results of mean film thickness as well as the corresponding value of U_a and Q into Eq. (2) and (4). Results show that f_i can be expressed as a monotropic function of Re_f, as shown in Fig. 7. A power correlation is obtained, giving an error of about ±20%, which is reliable given the experimental uncertainty involved (up to 5% at the case of minimum film thickness):

$$f_i = 0.106\,\mathrm{Re}_f^{\,-0.133} \tag{7}$$

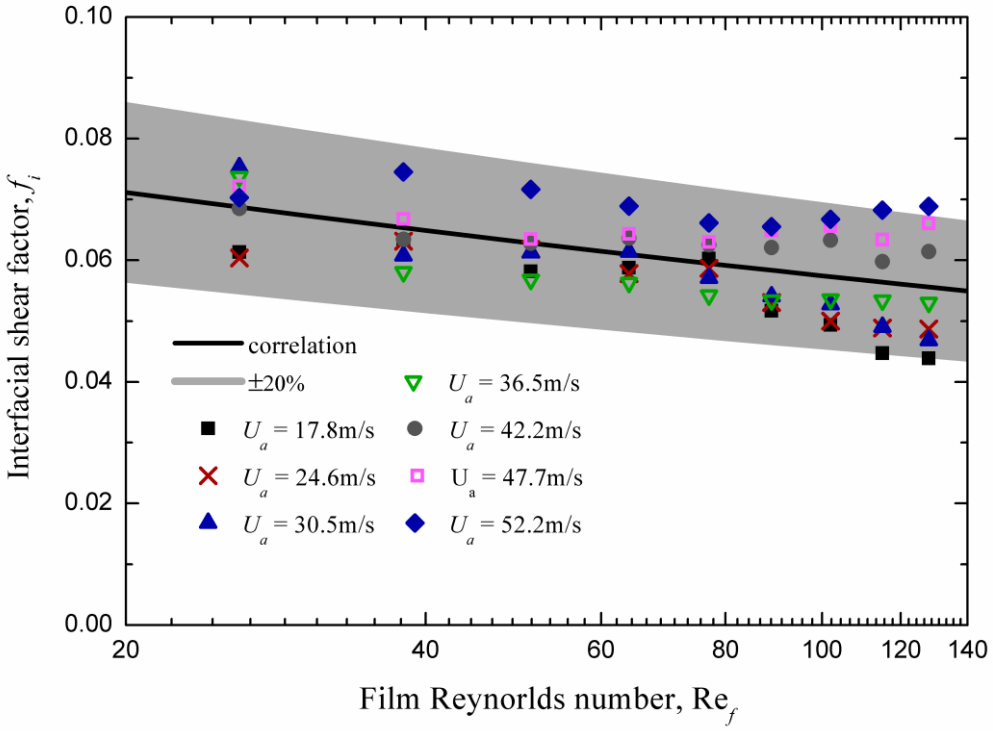

Fig. 7. Experimental data and correlation for interfacial shear factor.

A comparison was made between the present work and the predictions implemented in previous studies described in Section 2. The comparison with experimental results using wall friction factor (Eq. 5) for interfacial shear factor is plotted in Fig. 8(a), indicating that the mean film thickness is seriously over-predicted. It means that the effect of the shear stress is undervalued if the superficial fluctuations are neglected. As a consequence, the transport velocity of the water film will be slower than the actual value, and overmuch mass is evaluated as residual surface water.

Using the Stratified flow model in Eq. (6), Fig. 8(b) indicates that the prediction results are ameliorated compared to the case using wall friction factor. But the film thickness is still over-predicted; it indicates that the interfacial shear stress in the stratified flow experiment is relatively smaller than that of the present experiment. This may be explained by the different shapes of the solid substrate between the two experiments. In references, the working fluid generally flowed inside the tube or duct

and the liquid was limited by the side walls. The present experiment was conducted for a film flowing on a flat plane and the film was apart away from the side walls, which prevented the trend of liquid to gather.

Fig. 8(c) shows the prediction results using the proposed correlation of the interfacial shear factor, giving an overall relative error of ±20%. It indicates that the treatment on the interfacial shear stress used in the two-phase flow in the pipes, which separately consider the effect of the wind speed and flow rate, can also hold the flat flow sheared by high-speed gas stream. The magnitude of the interfacial shear stress acting on the surface of the water film flowing on a plate is proportional to the square of the value of the wind speed, and slightly dependent on the film Reynolds number.

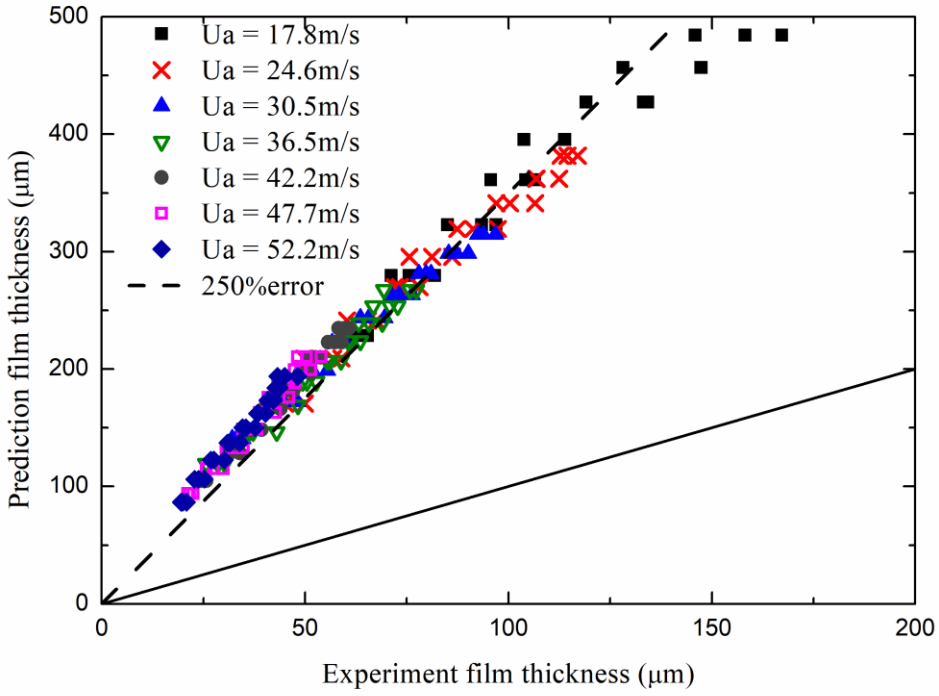

(a) Wall friction model using Eq.(5)

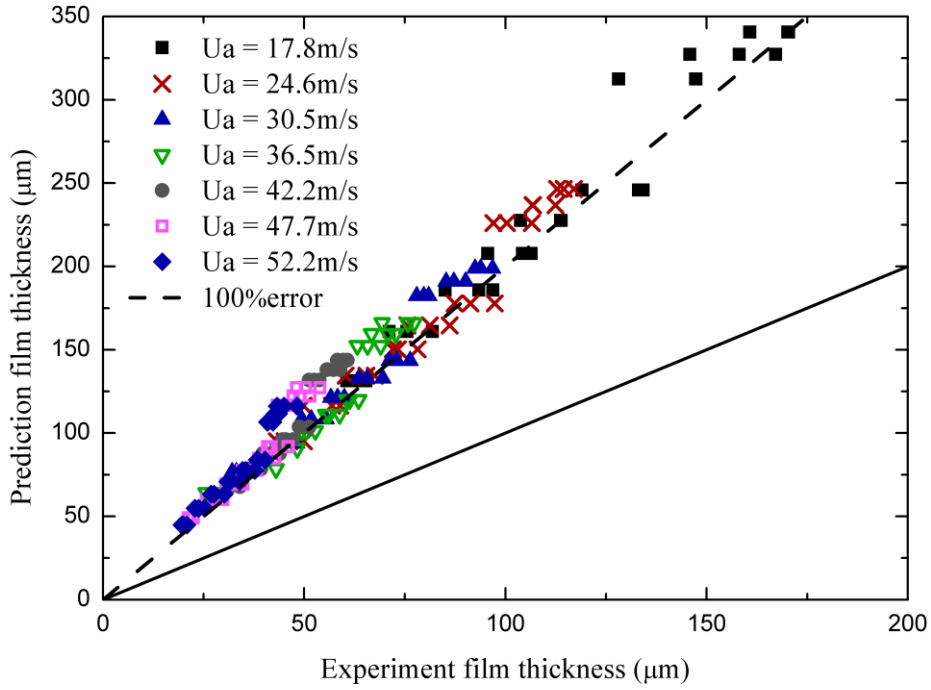

(b) Stratified flow model using Eq.(6)

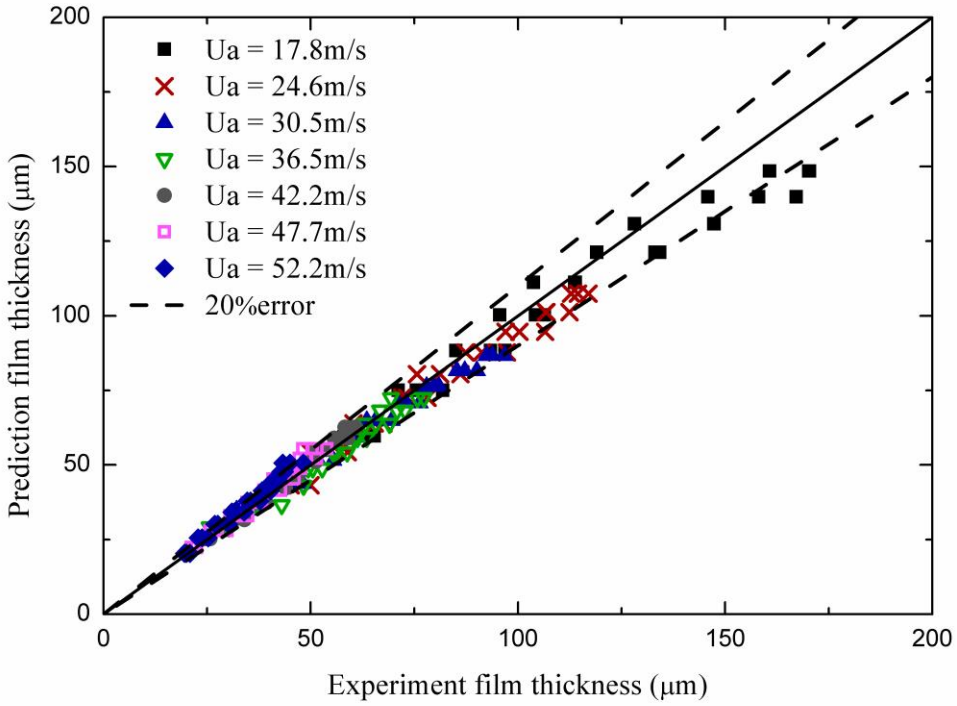

(c) Present model using Eq.(7)

Fig. 8. Comparison of the mean film thickness among the calculations with different correlations.

In order to evaluate the consistency with previous studies, the experimental results were compared with several models in the way of dimensionless film thickness $\delta+$, which was defined as

$$\delta^{+}=\frac{\rho_l u^{*}\overline{\delta}}{\mu_l} \tag{8}$$

where $u^{*}=\left(\tau_l/\rho_l\right)^{1/2}$ is the wall friction velocity defined using the shear stress τ_l inside the liquid film. Considering the force balance on a stable film flow, the shear stress across the film is equal to the interfacial shear stress. Thus the shear stress is obtained here using equation

$$\tau_l=\tau_i=0.053\mathrm{Re}_f^{-0.133}\cdot\rho_a U_a^2 \tag{9}$$

Based on a commonly used approximation in annular flow, referred to as the 'triangular relationship' between the time-averaged film thickness, the liquid flow rate and the average shear stress in film [26], it is postulated that when any two of the three variables are known, then it is possible to predict the third one. The values of δ^{+} and dimensionless liquid rate Re_f could be obtained from experimental data, and the relationship between them was plotted in Fig. 9. The present data are compared with some widely used prediction models, showing a good agreement. The application ranges of these models are presented in Table 1. The relationship derived by Kosky and Staub [46] considers an annular condense film in a horizontal tube, which is closest to the present conditions and gives the best prediction for the experimental results. Hughmark [47] model is based on the experiments of upward annular flow. It matches the present results when Re_f < 40, but over-predicts the results in the range of large film Reynolds numbers, that is thought attributed by the influence of the gravity. Asali's model [48], which is for a downward annular film flow under gas shear stress, has the same tendency with the present results, but the thickness of the downward film is overall smaller than that of horizontal flow.

Table 1. Dimensionless film thickness relations and their application range

Author	Application range	Re_f	Relation
Kosky & Staub	Horizontal condense flow	13-370	$\delta^+ = 1.316\,Re_f^{0.529}$
Hughmark	Upward flow	25-250	$\delta^+ = 0.874\,Re_f^{2/3}$
Asali	Vertical annular flow	20-300	$\delta^+ = 0.781 Re_f^{0.6}$
Present work	Horizontal plate flow	26-128	$\delta^+ = 1.292\,Re_f^{0.5289}$

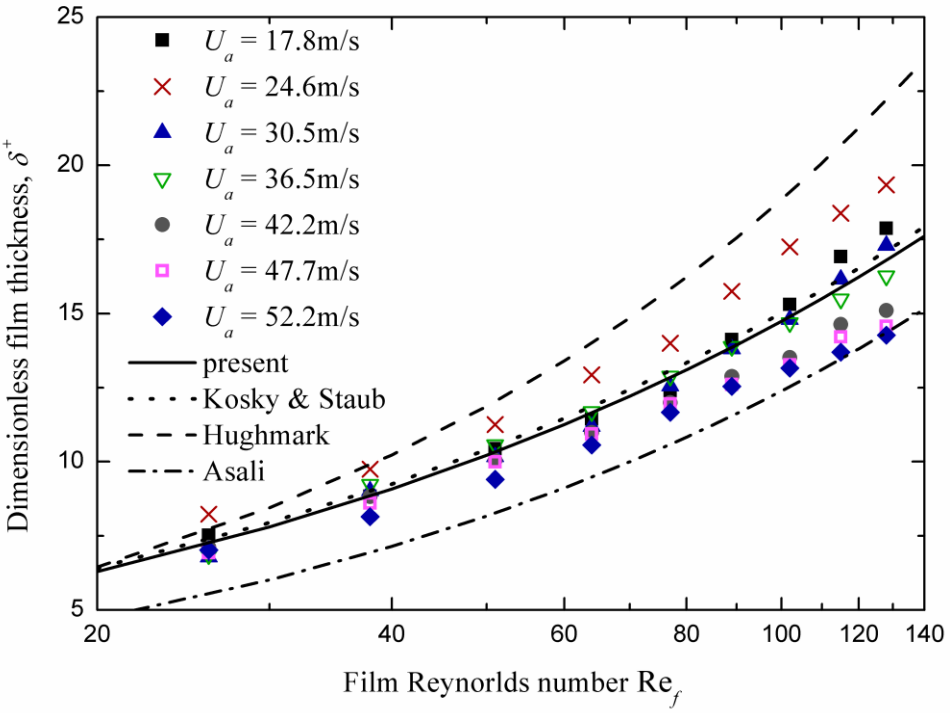

Fig. 9. Comparison of measured dimensionless film thickness with correlations.

An important characteristic of the intensity of the film fluctuations is the root-mean-square (RMS), which can be calculated using $\mathrm{RMS} = \left[\frac{1}{n}\sum_{i=1}^{n}\left(\delta_i - \overline{\delta}\right)^2\right]^{1/2}$, where n is the number of the collected values of the film thickness. Fig. 10 depicts the RMS results respectively as a function of (a) the wind speed U_a and (b) film Reynolds number Re_f. It can be seen that the variation trends of the roughness height are consistent with that of the mean film thickness, while the roughness varies more

intensely. The minimum value of RMS is about 7.6 μm, which is about a half of the minimum mean film thickness. Then RMS increased strongly with increasing Re_f and decreasing U_a due to the additional large amplitude waves, and became even a little higher than $\overline{\delta}$ in the cases of thick films. Therefore, it is reasonable to establish the correlations between the RMS and mean film thickness separately for the '3D wave' regime and 'roll wave' regime. Since the film thickness has an important effect on the wave parttern [49], $\overline{\delta}$ = 44 μm is selected as the transition point. Therefore, a piecewise linear relationship between the superficial roughness and mean film thickness can be employed as:

$$RMS_{global} = \begin{cases} 0.5\times\overline{\delta} & \overline{\delta} \le 44\mu m \\ 1.6\times\overline{\delta} - 48.4 & \overline{\delta} > 44\mu m \end{cases} \quad (10)$$

As shown in Fig. 11, the correlation gives a relative error within ±20%.

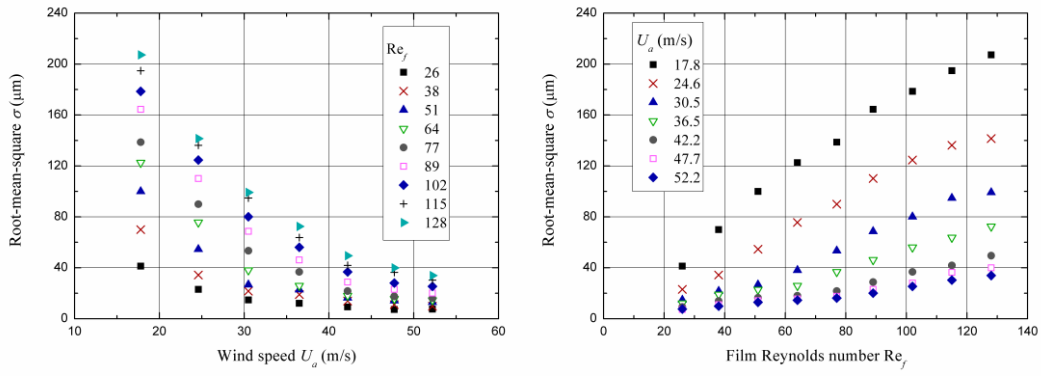

(a) (b)

Fig. 10. RMS of film fluctuations under different (a) wind speed U_a and (b) film Reynolds number Re_f.

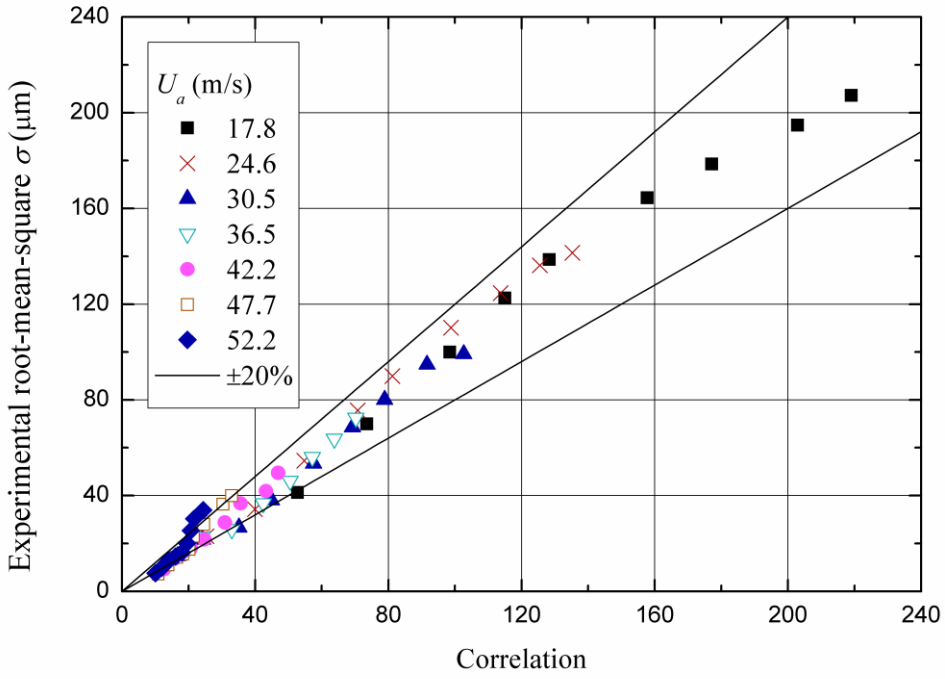

Fig. 11. Comparison of experimental values of RMS with predictions from the proposed correlation.

3.3. Statistical characteristic of waves

In order to provide detailed information on the shear-driven film and considering that new models regarding the interfacial wave may need support of the measured data (examples include surface roughness model and relating the instability of the ice growth rate with the interfacial waves), this paper presents a quantified statistical work on the waves. The statistical study of the waves has been obtained in two ways: ① by carrying out a power spectral density (PSD) analysis on the film thickness signals and ② by division of the film thickness data between underlying film and large waves.

3.3.1. Spectrum analysis

The dominant frequency of the film thickness signal were obtained by PSD analysis on the temporal film thickness traces such as those in Figs. 3 and 4. The PSD procedure was implemented using standard functions in MATLAB R2010a, and typical results of the spectrum analysis were plotted in Fig. 12: black lines for the

distribution of PSDs without windowed and averaged process, while red lines for the results using Welch's averaged periodogram method with Hamming window. Obviously the red lines retained the distribution characteristic of PSD, and emphasized the locations of the peak value as well, thus preferred for post-processing and quantitative analysis [26].

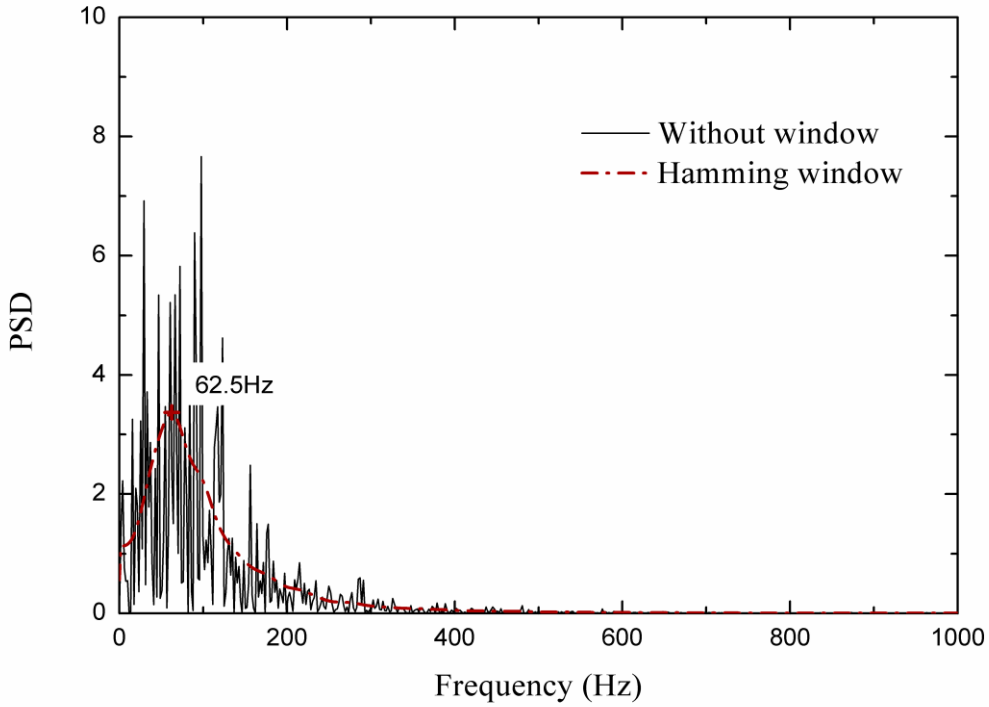

(a)

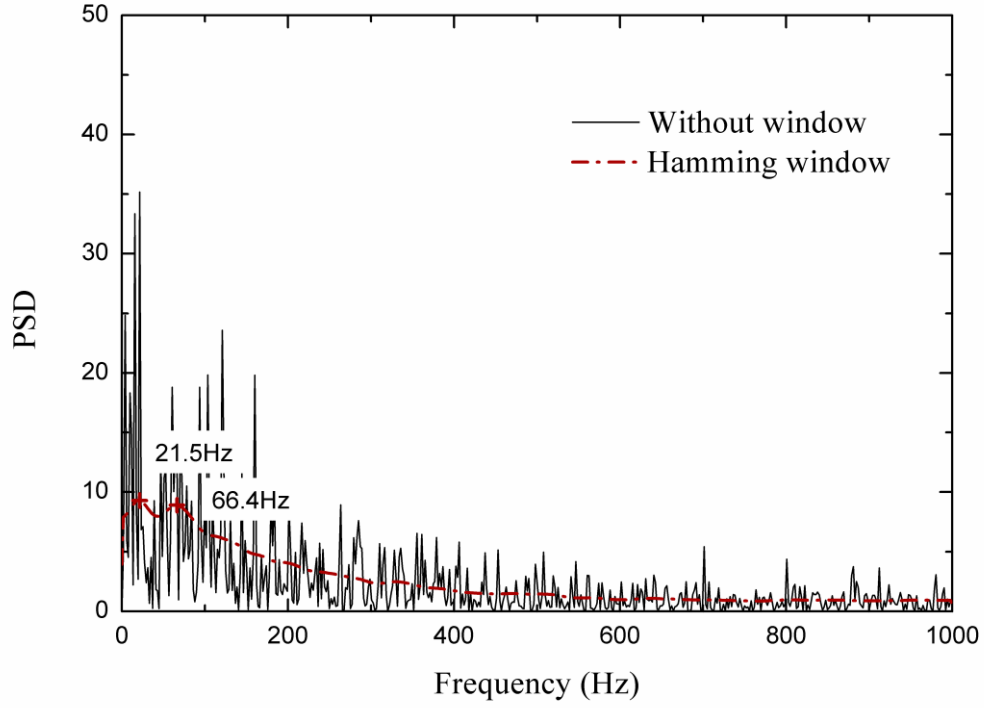

(b)

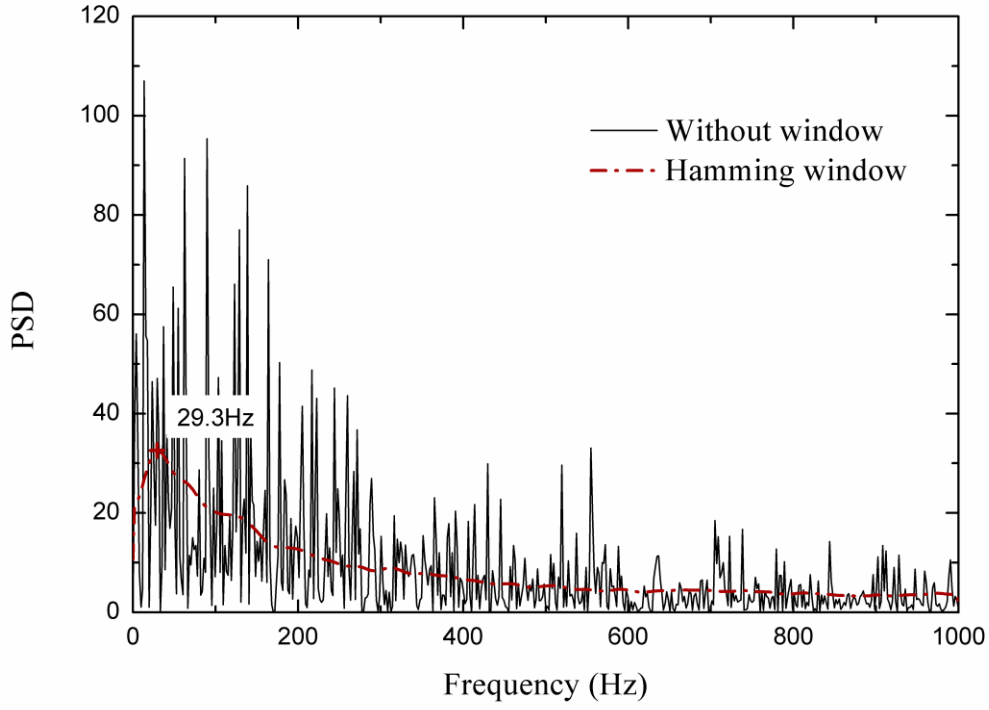

(c)

Fig. 12. Samples of power spectral density (PSD) for wind speed of 30.5m/s and:

(a) Re_f =38.3; (b) Re_f =76.7; (c) Re_f =115.0.

It is accepted that the frequency of the PSD peak corresponds to the waves carrying the highest amount of the energy in the shape of the liquid film interface. However, extra identification is needed to identify whether the frequency belongs to the larger amplitude waves (roll wave) or the more frequent, but smaller amplitude waves (ripples), when the two types of waves occur at the same time. For example, Zadrazil et al. [24] observed that the PSD peak frequency corresponds more closely to the ripples, while Setyawan et al. [50] attributed the PSD peak frequency to the frequency of the large amplitude waves. Using the temporal film thickness traces in Fig. 3 for the comparison, the PSD results in Fig. 12 show that at Re_f = 38 the waves of the peak power frequency (62.5 Hz) is obviously the ripples and at Re_f = 115 is the large waves (29.5Hz) with a constant wind speed of 30.5 m/s. It is interesting to observe that the transition between the two situations happens at Re_f = 77, when two peaks coexist in the PSD distribution curve.

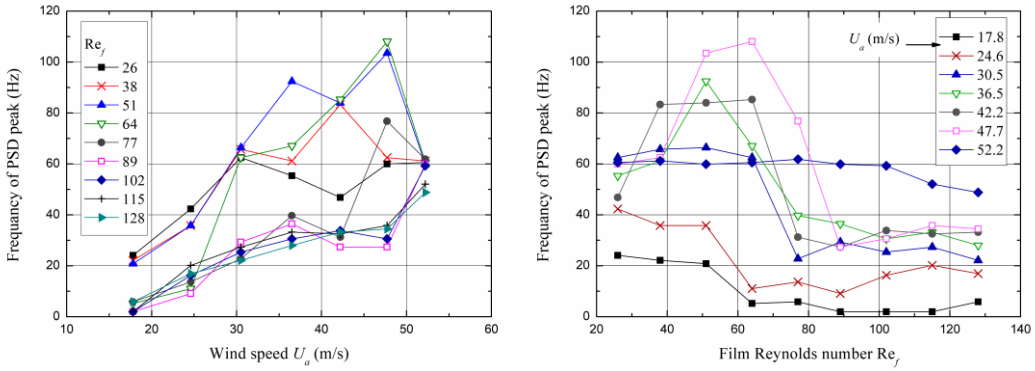

(a) (b)

Fig. 13. Peak power frequency f_{pp} under different (a) wind speed U_a and (b) film Reynolds number Re_f.

Overall data for the peak frequency obtained from each PSD analysis and the averaged results of the triplicate experiments are shown in Fig. 13 as a function of (a) wind speed U_a and (b) film Reynolds number Re_f. It is observed that the wind speed plays a more important role in influencing the peak power frequency f_{pp} than the liquid Reynolds number Re_f, and the peak power frequency generally increases with

increased wind speed. The frequency values can be divided into two groups attributed to the change of the flow regimes: the higher frequencies are exhibited in the '3D wave' regime, whereas the lower in the 'roll wave' regime. Besides, for lower wind speed, the transition of f_{pp} occurs at a smaller value of Re_f, and the value of the transition Reynolds number gradually increases when U_a rises, which showed the same trend with the transition of the flow regime. An exception is the cases of U_a = 52.2 m/s, where the ripples dominate in the shape of the liquid film interface. Since the spectral signatures reported by PSDs correspond to the full wave content, covering the full range from ripples to roll waves, it is difficult to identify the contribution share from each type of the wave. The PSD analysis provides a general understanding, but is insufficient in reconstruction of the fluctuations in shape.

3.3.2. Underlying film and ripples

From the viewpoint of the instantaneous thickness, the interfacial structure can be seen as the combination of underlying film with ripples and irregular large waves. The idea behind the sections 4.3.2 ~ 3 is to separate these two structures, and respectively study their variations with the wind speed or film Reynolds number. A concept named substrate thickness δ_{sub} is introduced for the separation threshold, which is defined as the thickness appears most frequently. It means δ_{sub} is the thickness corresponding to the peak value of the probability density function (PDF). The definitions of the thicknesses: substrate thickness δ_{sub}, mean film thickness $\overline{\delta}$, and the thickness of large waves δ_{LW}, are drawn in Fig. 14. It was found that the substrate thickness is more unchangeable with the amount of the large waves, and more suitable for identification than the mean film thickness. After a prior work of the test and comparison, the value of three times the substrate thickness δ_{sub} was selected as threshold in this work. It is confirmed that the results were not sensitive to the choice of the amplitude threshold factor within a range of 2.8~3.5.

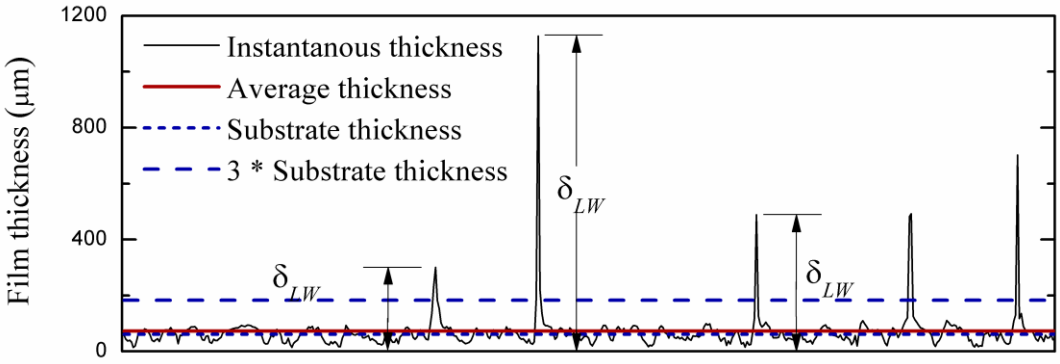

Fig. 14. Sketch of film flow and various thicknesses.

In Fig. 15, (a) the substrate thickness and (b) the roughness of ripples were presented as a function of the film Reynolds number Re_f. The roughness of ripples was defined as the RMS results of the film thickness traces despite of the large waves. Similarly, both the substrate thickness and roughness of the ripples monotonically increase with the increasing Re_f and decreasing U_a. When compared with the mean film thickness $\overline{\delta}$ and superficial roughness, the substrate thickness δ_{sub} and roughness of the underlying film show smaller change with increasing film Reynolds number. The difference between $\overline{\delta}$ and δ_{sub} is within 8 μm for the cases of '3D wave' flow. The difference becomes obvious in 'roll wave' regime, since the substrate thickness is almost independent of the large waves, and the maximum gap between them reaches 84 μm. It shows that the water film flows in '3D wave' regime can be regarded as the flow of underlying film. As an inheritance of the correlation between the RMS_{global} and $\overline{\delta}$ (Eq. (14)), the relationship between δ_{sub} and RMS_{ripple} is the same with that in the part of '3D wave' regime. The roughness of the ripples can be seen as half of the substrate thickness, giving relative error of 20%, as shown in Fig. 16.

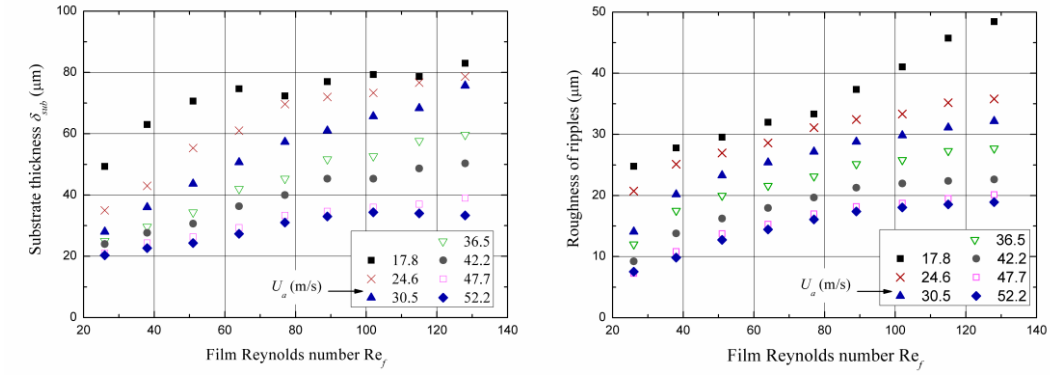

(a) (b)

Fig. 15. (a) Substrate film thickness and (b) RMS of ripples as functions of film Reynolds number Re_f.

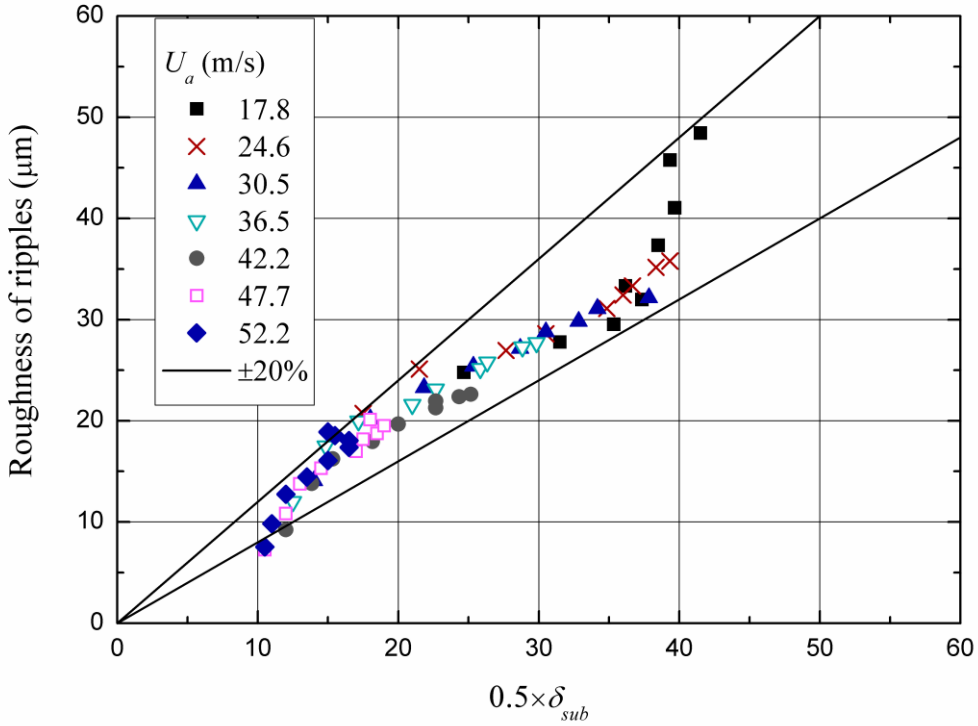

Fig. 16. Comparison of experimental RMS of ripples with predictions from the proposed correlation.

3.3.3. Large waves

The statistical results of the large waves make sense only in 'roll wave' regime, when the frequency of the large waves is larger than 5; therefore, the points in '3D

wave' regime were ignored in following figures. Fig. 17 separately shows the frequency of the large waves as a function of (a) wind speed U_a, and (b) film Reynolds number Re_f. For the variation with wind speed, it is found that the trends in frequency counting do not completely match the trends in literature [25], which found that the frequency of the roll waves monotonically increased with U_a when Re_f is in the range of 155 ~ 520. In the present experiment, the frequency of the large waves firstly decreases with increasing U_a, due to the acceleration of the underlying water film and ripples. The frequency reaches the minimum at about U_a = 40 m/s, and then increases slightly with the increase of U_a. It might implies that the flow has not entered into the core of the roll wave regime until wind speed is beyond 40 m/s in the range of Re_f < 128. As indicated in Fig. 17(b), the frequency of the large waves increased monotonously with increasing film Reynolds number, while the amplitude shows nearly independent on Re_f as shown in Fig. 18(b). It can be explained by that as the inlet liquid flow rate increases, the large waves will carry more amount of liquid through adding the number of the disturbances.

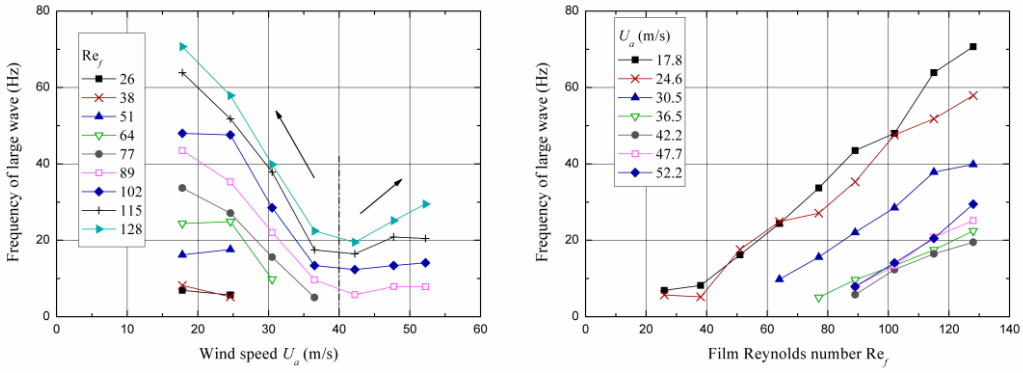

(a) (b)

Fig. 17. Frequency of large amplitude waves under different (a) wind speed U_a and (b) film Reynolds number Re_f.

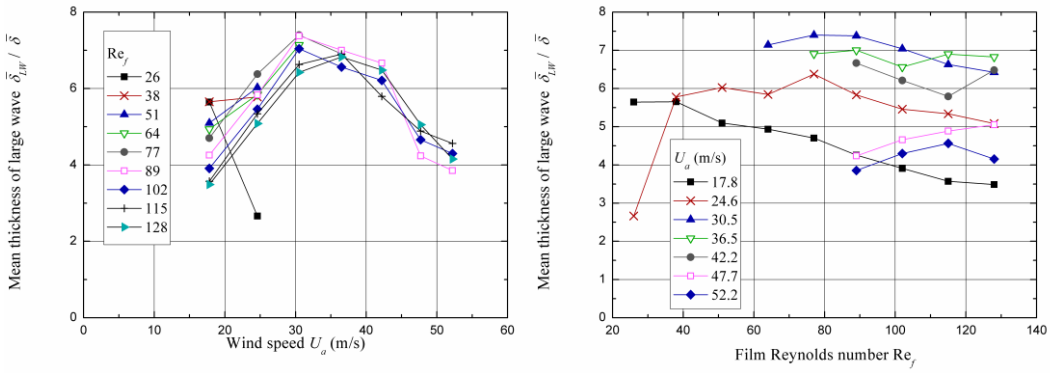

(a) (b)

Fig. 18. Mean amplitude normalized by the mean film thickness under different (a) wind speed U_a and (b) film Reynolds number Re$_f$.

Fig. 18 depicted the mean amplitudes of the large waves normalized by mean film thickness from Fig. 4. The normalized thickness of the large waves attained the values within the range 4~8 and a maximum appeared at intermediate U_a. An exceptional point is the case of U_a = 24.6 m/s and Re$_f$ = 26, at which the frequency of the large waves is the most close to 5; thus the value of the large wave amplitude at this point may not perfectly reflect the thickness of the roll waves.

4. Conclusions

An experimental study was reported of the shear-driven water film flows on an aluminum substrate for the sake of the supplement for the aerodynamic icing and anti-icing modeling. The flow structures of the film were identified visually and by statistical analysis of the film thickness measurements. The variations of the local instantaneous thickness, as well as the statistical characteristics of the film (mean film thickness, superficial roughness (RMS), power spectrum density, frequency and amplitude of waves) with the wind speed and film Reynolds number were obtained and analyzed.

The experimental results of the mean film thickness were compared with that of two popular prediction models. Results showed that the previous models using

substitute calculations for interfacial shear factor over-predicted the mean film thickness. It was considered due to the differences in the superficial wave and experiment solid substrate. A new correlation of the interfacial shear factor to obtain the mean film thickness was proposed. Good agreement was achieved between the present results and the models from annular flow experiments after dimensionless process. The superficial roughness, expressed as RMS of film thickness, was found highly dependent on mean film thickness, and a piecewise linear relationship between them is employed.

Spectrum analysis of the film thickness signal indicated that the frequencies of the PSD peaks preferred to vary with the wind speed rather than film Reynolds number. But spectrum analysis showed a sort of incoherency between the peak frequencies due to the transition of the flow pattern. Based on the identification of the flow structure, comprehensive analysis on the waves was presented by division of the film thickness data between underlying film and large waves. For the underlying film, it was found that the correlation between the roughness of the ripples and substrate thickness was consistent with the correlation between the superficial roughness and mean film thickness. For the large waves, the frequency monotonically increased with increasing film Reynolds number, while a transition point was observed in the variation of frequency with wind speed, which could be explained as the beginning of full-developed ‘roll wave’ regime; the amplitudes of large wave were normalized by the mean film thickness, with the value in the range of 4~8.

Acknowledgements

This work was financially supported by National Basic Research Program of China under Grants No. 2015CB755803.

References:

[1] R.W. Gent, N.P. Dart, and J.T. Cansdale, Aircraft icing. Philosophical Transactions of the

Royal Society A: Mathematical, Physical and Engineering Sciences 358 (2000) 2873-2911.

[2] O. Parent, and A. Ilinca, Anti-icing and de-icing techniques for wind turbines: Critical review. Cold Regions Science and Technology 65 (2011) 88-96.

[3] E.A. Whalen, A.P. Brocren, and M.B. Bragg, Aerodynamics of scaled runback ice accretions. JOURNAL OF AIRCRAFT 45 (2008) 591-603.

[4] C. Wang, S. Chang, M. Leng, H. Wu, and B. Yang, A two-dimensional splashing model for investigating impingement characteristics of supercooled large droplets. International Journal of Multiphase Flow 80 (2016) 131-149.

[5] J.T. Streitz, and R. Ettema, Observations from an aufeis windtunnel. Cold Regions Science and Technology 34 (2002) 85-96.

[6] B.L. Messinger, Equilibrium Temperature of an Unheated Icing Surface as a Function of Air Speed. Journal of the Aeronautical Sciences 20 (1953) 29-42.

[7] R.J. Hansman, and S.R. Turnock, Investigation of surface water behavior during glaze ice accretion. Journal of Aircraft 26 (1989) 140-147.

[8] R.J. Hansman, K. Yamaguchi, B. Berkowitz, and M. Potapczuk, Modeling of surface roughness effects on glaze ice accretion. Journal of thermophysics and heat transfer 5 (1991) 54-60.

[9] G. Fortin, J.L. Laforte, and A. Ilinca, Heat and mass transfer during ice accretion on aircraft wings with an improved roughness model. International Journal of Thermal Sciences 45 (2006) 595-600.

[10] K.M. Al-Khalil, Jr. T.G. Keith, and K.J. De Witt, Development of an improved model for runback water on aircraft surfaces. JOURNAL OF AIRCRAFT 31 (1994) 271-278.

[11] G. Fortin, A. Ilinca, J. Laforte, and V. Brandi, New Roughness Computation Method and Geometric Accretion Model for Airfoil Icing. Journal of Aircraft 41 (2004) 119-127.

[12] S. Moghtadernejad, M. Jadidi, M. Tembely, N. Esmail, and A. Dolatabadi, Concurrent Droplet Coalescence and Solidification on Surfaces with Various Wettabilities. Journal of Fluids Engineering 137 (2015) 071302-1-071302-10.

[13] E.B. White, and J.A. Schmucker, A Runback Criterion for Water Drops in a Turbulent

Accelerated Boundary Layer. Journal of Fluids Engineering 130 (2008) 061302-1-061302-6-0.

[14] G. McAlister, R. Ettema, and J.S. Marshall, Wind-Driven Rivulet Breakoff and Droplet Flows in Microgravity and Terrestrial-Gravity Conditions. Journal of Fluids Engineering 127 (2005) 257-266.

[15] S. Moghtadernejad, M. Jadidi, A. Dolatabadi, and N. Esmail, SPH Simulation of Rivulet Dynamics on Surfaces with Various Wettabilities. SAE International Journal of Aerospace 8 (2015) 160-173.

[16] A. Feo, and J. Tsao, The Water Film Weber Number in Glaze Icing Scaling, SAE Aircraft & Engine Icing International Conference, Seville, Spain, 2007, pp. 14.

[17] T. Muzik, P. Safarik, and A. Tucek, Analysis of the water film behavior and its breakup on profile using experimental and numerical methods. Journal of Thermal Science 23 (2014) 325-331.

[18] J. Alzaili, and D. Hammond, Experimental Investigation of Thin Water Film Stability and Its Characteristics in SLD Icing Problem, SAE 2011 International Conference on Aircraft and Engine Icing and Ground Deicing, Chicago, Illinois, USA, 2011, pp. 6.

[19] K. Zhang, J. Blake, R. Alric, and H. Hu, An Experimental Investigation on Wind-Driven Rivulet/Film Flows over a NACA0012 Airfoil by Using Digital Image Projection Technique, AIAA SciTech forum, National Harbor, MD, 2014, pp. 9.

[20] K. Zhang, T. Wei, and H. Hu, An experimental investigation on the surface water transport process over an airfoil by using a digital image projection technique. Experiments in Fluids 56 (2015) 173.

[21] Y.Q. Yu, and X. Cheng, Experimental study of water film flow on large vertical and inclined flat plate. Progress in Nuclear Energy 77 (2014) 176-186.

[22] Y. Yoshinaga, H. Peng, C. Dang, and E. Hihara, Experimental Study on Liquid Film Thickness of Annular Flow in Microchannels, 15th International Refrigeration and Air Conditioning Conference, Purdue, 2014.

[23] D.W. Zhou, T. Gambaryan-Roisman, and P. Stephan, Measurement of water falling film thickness to flat plate using confocal chromatic sensoring technique. Experimental Thermal and

Fluid Science 33 (2009) 273-283.

[24] I. Zadrazil, O.K. Matar, and C.N. Markides, An experimental characterization of downwards gas – liquid annular flow by laser-induced fluorescence: Flow regimes and film statistics. International Journal of Multiphase Flow 60 (2014) 87-102.

[25] A.V. Cherdantsev, D.B. Hann, and B.J. Azzopardi, Study of gas-sheared liquid film in horizontal rectangular duct using high-speed LIF technique: Three-dimensional wavy structure and its relation to liquid entrainment. International Journal of Multiphase Flow 67 (2014) 52-64.

[26] Y. Zhao, C.N. Markides, O.K. Matar, and G.F. Hewitt, Disturbance wave development in two-phase gas – liquid upwards vertical annular flow. International Journal of Multiphase Flow 55 (2013) 111-129.

[27] S.H. Pham, Z. Kawara, T. Yokomine, and T. Kunugi, Measurements of liquid film and droplets of annular two-phase flow on a rod-bundle geometry with spacer. International Journal of Multiphase Flow 70 (2015) 35-57.

[28] A. Bonilla Riaño, I.H. Rodriguez, A.C. Bannwart, and O.M.H. Rodriguez, Film thickness measurement in oil – water pipe flow using image processing technique. Experimental Thermal and Fluid Science 68 (2015) 330-338.

[29] F. Touron, L. Labraga, L. Keirsbulck, and H. Bratec, Measurements of liquid film thickness of a wide horizontal co-current stratified air-water flow. Thermal Science 19 (2015) 521-530.

[30] T. Myers, and C. Thompson, Modeling the flow of water on aircraft in icing conditions. AIAA Journal 36 (1998) 1010-1013.

[31] T. Myers, J. Charpin, and C. Thompson, Slowly accreting ice due to supercooled water impacting on a cold surface. PHYSICS OF FLUIDS 14 (2002) 240-256.

[32] O. Harireche, P. Verdin, C.P. Thompson, and D.W. Hammond, Explicit Finite Volume Modeling of Aircraft Anti-Icing and De-Icing. Journal of Aircraft 45 (2008) 1924-1936.

[33] D. Yanxia, G. Yewei, X. Chunhua, and Y. Xian, Investigation on heat transfer characteristics of aircraft icing including runback water. International Journal of Heat and Mass Transfer 53 (2010) 3702-3707.

[34] Y. Cao, J. Huang, and J. Yin, Numerical simulation of three-dimensional ice accretion on an

aircraft wing. International Journal of Heat and Mass Transfer 92 (2016) 34-54.

[35] W. Wright, P. Struk, T. Bartkus, and G. Addy, Recent Advances in the LEWICE Icing Model, SAE 2015 International Conference on Icing of Aircraft, Engines, and Structures, Prague, Cezch Republic, 2015, pp. 9.

[36] A.R. Karev, M. Farzaneh, and E.P. Lozowski, Character and stability of a wind-driven supercooled water film on an icing surface—I. Laminar heat transfer. International Journal of Thermal Sciences 42 (2003) 481-498.

[37] K. Ueno, and M. Farzaneh, Linear stability analysis of ice growth under supercooled water film driven by a laminar airflow. Physics of Fluids 23 (2011) 042103.

[38] A.P. Rothmayer, and H. Hu, Solutions for Two-Dimensional Instabilities of Ice Surfaces Uniformly Wetted by Thin Films, AIAA atmospheric and space environments conference, New Orleans, LA(US), 2012, pp. 17.

[39] G. Wang, and A.P. Rothmayer, Thin water films driven by air shear stress through roughness. Computers & Fluids 38 (2009) 235-246.

[40] M. Ishii, and M.A. Grolmes, Inception criteria for droplet entrainment in two-phase concurrent film flow. AlChE Journal 21 (1975) 308-318.

[41] N.P. Cheremisinoff, and E.J. Davis, Stratified turbulent - turbulent gas - liquid flow. AIChE journal 25 (1979) 48-56.

[42] N. Andritsos, and T.J. Hanratty, Influence of interfacial waves in stratified gas - liquid flows. AIChE journal 33 (1987) 444-454.

[43] S.V. Paras, N.A. Vlachos, and A.J. Karabelas, Liquid layer characteristics in stratified—Atomization flow. International journal of multiphase flow 20 (1994) 939-956.

[44] W.Y. Wu, Fluid Dynamics, Peking University Press, 2004.

[45] M. Miya, D.E. Woodmansee, and T.J. Hanratty, A model for roll waves in gas-liquid flow. Chemical Engineering Science 26 (1971) 1915-1931.

[46] P.G. Kosky, and F.W. Staub, Local condensing heat transfer coefficients in the annular flow regime. AIChE Journal 17 (1971) 1037-1043.

[47] G.A. Hughmark, Film thichness, entrainment, and pressure drop in upward annular and

dispersed flow. AIChE Journal 19 (1973) 1062-1065.

[48] J.C. Asali, T.T. Hanratty, and P. Andreussi, Interfacial drag and film height for vertical annular flow. AIChE Journal 31 (1985) 895-902.

[49] A.D. Craik, Wind-generated waves in thin liquid films. Journal of Fluid Mechanics 26 (1966) 369-392.

[50] A. Setyawan, Indarto, and Deendarlianto, The effect of the fluid properties on the wave velocity and wave frequency of gas – liquid annular two-phase flow in a horizontal pipe. Experimental Thermal and Fluid Science 71 (2016) 25-41.